Construction and Building Materials 366 (2023) 130163

Contents lists available at ScienceDirect

Construction and Building Materials

journal homepage: www.elsevier.com/locate/conbuildmat

Structural behaviour of post-installed reinforcement for 3D concrete printed shells – A case study on water tanks

Lukas Gebhard [a,*], Jaime Mata-Falcón [b], Arsalan Iqbal [c], Walter Kaufmann [d]

[a] Institute of Structural Engineering, ETH Zurich, Stefano-Franscini-Platz 5, 8093 Zurich, Switzerland
[b] Institute of Structural Engineering, ETH Zurich, Stefano-Franscini-Platz 5, 8093 Zurich, Switzerland
[c] Knauf Gips KG, Am Bahnhof 7, 97346 Iphofen, Germany
[d] Institute of Structural Engineering, ETH Zurich, Stefano-Franscini-Platz 5, 8093 Zurich, Switzerland

ARTICLE INFO

Keywords:
Digital fabrication
3D concrete printing
Post-installed reinforcement
Eccentric reinforcement
Tensile tests

ABSTRACT

Incorporating sufficient reinforcement to ensure a ductile structural behaviour is a persisting challenge in digitally fabricated concrete structures. This paper investigates the structural performance of a reinforcement approach for 3D concrete printed elements, consisting of an unreinforced 3D printed concrete shell and a sprayed shell reinforced with a conventional reinforcing mesh for application in water tanks. Four reinforced concrete elements produced with this approach were tested in direct tension and compared to a reference test of a monolithic specimen to analyse the behaviour of circular water tanks under hoop stresses. Two eccentric reinforcement arrangements and two different printing patterns were investigated. Despite the testing setup not perfectly representing the actual behaviour of circular water tanks, in which shell deformations are kinematically restrained, the feasibility of the fabrication method could be examined. The results did not show significant differences in the behaviour of the different fabrication methods, with similar ductility as expected in a conventionally reinforced shell. The eccentric reinforcement caused the crack formation to originate on the surface close to the reinforcement, accompanied by out-of-plane deformations. The cracks on the far side of the reinforcement opened suddenly and reduced the out-of-plane deformations. The predictions with models neglecting the eccentricity of the reinforcement overestimated the crack opening. The best predictions were obtained from the tension chord model by only considering the concrete area defined by twice the mechanical cover of the reinforcement.

1. Introduction

The construction industry needs to change drastically to face the current challenges of climate change and the simultaneous increase in the world population. With the need for more sustainable construction, industry and academia are developing new materials and processes. One of these areas is digital fabrication with concrete [1], which aims at developing fully or partly automated concrete construction processes [2]. One of the most prominent technologies is 3D concrete printing (3DCP) [3]. Concrete elements are produced layer by layer in this fabrication approach through an extrusion process. However, the application of 3DCP is currently limited to structurally low-demanding elements, which are essentially equivalent to masonry walls [4,5] in terms of load-bearing capacity. One of the main limitations to reaching a broader application of 3DCP is the lack of reinforcement strategies, which has recently been addressed in studies proposing possible solutions [4,6–8]. A promising reinforcement strategy with a large potential for reinforced wall elements (i.e. shells) is the printing of an unreinforced shell and the subsequent placement and fixation of reinforcement meshes. The fixation of the mesh can either be done by subsequent spraying or extrusion [7–11]. The advantage of this process lies in separating the printing and the reinforcing processes while still resulting in a fully reinforced element. Furthermore, conventional reinforcing meshes can be applied, making a design compliant with conventional building codes straightforward. However, the geometrical flexibility is limited since the geometry needs to allow the separate placement and fixation of the reinforcement mesh. For a positive impact of 3DCP, applications need to be identified where (i) the geometrical flexibility of the process is capitalised, (ii) waste and material consumption can be

* Corresponding author.
E-mail addresses: gebhard@ibk.baug.ethz.ch (L. Gebhard), mata-falcon@ibk.baug.ethz.ch (J. Mata-Falcón), Arsalan.Iqbal@knauf.com (A. Iqbal), kaufmann@ibk.baug.ethz.ch (W. Kaufmann).

https://doi.org/10.1016/j.conbuildmat.2022.130163
Received 5 October 2022; Received in revised form 12 December 2022; Accepted 20 December 2022
Available online 14 January 2023

Nomenclature

A_c	Area of concrete cross-section
A_s	Area of reinforcing steel cross-section
E_c	Young's modulus of concrete
E_s	Young's modulus of reinforcing steel
F	Total applied load
IS	Inside face
OS	Outside face
SV	Sideview
c	Concrete cover
f_c	Concrete compressive strength
f_{ct}	Concrete tensile strength
$f_{ct,eff}$	Effective concrete tensile strength
f_{ctm}	Mean concrete tensile strength
f_{su}	Ultimate strength of reinforcing steel
f_{sy}	Yield strength of reinforcing steel
k	Factor for $s_{r,\max}$ considering the concrete cover
$k_{1\text{-}4}$	Factors for $s_{r,\max}$
$k_{a\text{-}c}$	Fitting factors
k_t	Factor of the loading condition
s_{r0}	Crack spacing
s_{rm}	Mean crack spacing
$s_{r,\max}$	Maximum crack spacing
$s_{r,\min}$	Minimum crack spacing
w_i	Crack opening on the inside surface
w_{k1}	Crack opening limitation
w_o	Crack opening on the outside surface
w_r	Crack opening
Δ	Displacements
β	Factor of the loading condition
ε	Tensile strains
ε_{cm}	Mean strain of the concrete
ε_{sh}	Hardening strain of reinforcing steel
ε_{sm}	Mean tensile strain of reinforcing steel
ε_{su}	Ultimate strain of reinforcing steel
ε_{sy}	Yield strain of reinforcing steel
λ	Factor for the crack spacing
σ	Tensile stresses
σ_{sr}	Reinforcing stresses at the crack
σ_{sr0}	Reinforcing stresses at cracking
τ_{b0}	Bond strength before yielding
τ_{b1}	Bond strength after yielding
ρ_s	Reinforcement ratio
Ø	Reinforcing bar diameter

reduced, and hence (iii) the reinforcement strategy offers a clear benefit.

The walls of reinforced concrete tanks for water storage combine these aspects and are, thus, ideally suited as a pilot application. Concrete water tanks are an efficient way to store large volumes of liquids. They are typically rectangular or circular in plan and can be found above ground, partly emerged or entirely underground [12]. Circular tanks are particularly efficient, carrying the main load (hydrostatic pressure) by circumferential tension. Fig. 1a shows the typical layout of a circular tank with a thick floor slab, a circular wall and a roof slab. Support columns for the roof slab are added in the centre for large-diameter tanks. The typical wall reinforcement layout for a tank with a diameter of 10 m and a height of 4 m can be seen in Fig. 1b. For conventional construction, the inner formwork is installed first. Afterwards, the two layers of prefabricated meshes are added, and the outer formwork is placed. Subsequently, the concrete is cast in multiple steps until the final height is reached. This fabrication approach is time-consuming and requires different formwork arrangements for different tank diameters, as well as minimum wall thicknesses (with correspondingly higher minimum reinforcement) to ensure the placement and proper compaction of the concrete.

Therefore, new fabrication methods such as 3DCP might offer an alternative for fabricating concrete water tanks with reduced limitations on geometric freedom. For this fabrication approach, a process is envisaged where first, an unreinforced inner shell of the tank is printed. Afterwards, one reinforcement mesh is placed around the printed shell and sprayed with concrete. Fig. 1c illustrates the resulting cross-section of such a wall. Applying this fabrication process (i) reduces the amount of different formwork for different tank diameters, (ii) enables a smaller wall thickness and (iii) might only require reinforcement on the outside of the printed wall part since the dominant load case (hydrostatic pressure) can be carried by hoop stresses on the outside.

Large-scale structural tests are required to assess the viability of new fabrication approaches [13–15], given that they usually differ significantly from existing experimental evidence on conventional concrete structures. The behaviour of shells with eccentrically placed reinforcement and the uncertainties due to the mechanical interaction of 3D

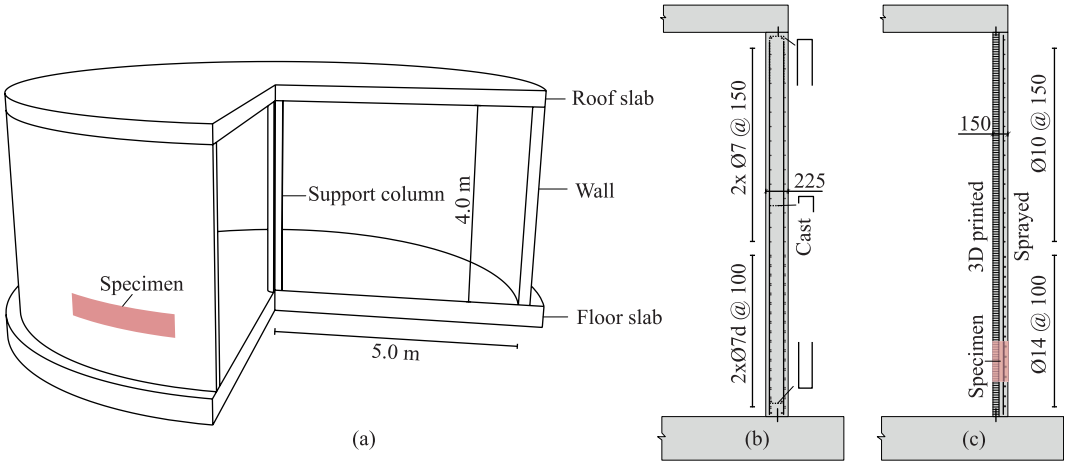

Fig. 1. Circular concrete water tank: (a) three-quarters of a wall tank structure; (b) reinforcement layout of a conventional water tank wall; (c) reinforcement layout of a 3D concrete printed and sprayed water tank wall (dimensions in [mm]).

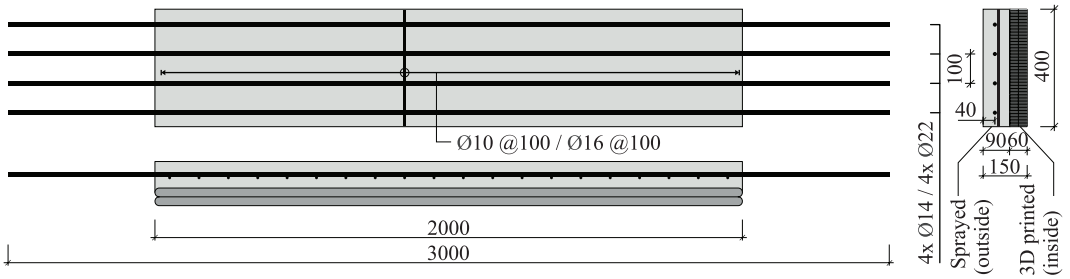

Fig. 2. Nominal geometry and reinforcement layout of the specimens. The cross-sections are particularised for the straight printing pattern. (dimensions in [mm]).

printed and sprayed concrete are two characteristic aspects of the solution under analysis for which testing is required to ensure a safe and predictable structural performance. For a mass market application, the results of the tests need to be predictable with well-established design concepts, so further produced elements do not need to be tested. This paper presents a feasibility study of the structural performance of circular water tanks, in which effects introduced due to the circularity, such as internal restraints and radial pressure, are neglected.

2. Research significance

Spraying concrete on top of unreinforced printed shells after placing (conventional) reinforcement on the shell enables the fabrication of large-scale reinforced shell elements. These shells could be applied to other load-bearing elements that require only one layer of reinforcement. A similar fabrication approach could also be applied for two symmetric layers of reinforcement to extend the range of applications. However, this consideration is outside the scope of this study. For the structural performance assessment, the case study of water tanks was investigated. A previous study on the automatisation of water tank production had shown the potential of the proposed fabrication approach for this type of structure [16]. However, the mechanical performance and water tightness of tank walls with (i) two different concrete types with a cold joint and (ii) only one layer of eccentric reinforcement cannot be predicted with conventional design approaches. These walls carry loads primarily in the circumferential direction (i.e. along the wall), where tensile hoop stresses (which can be determined by Barlow's formula) are caused by hydrostatic pressure. Therefore, an experimental campaign on straight specimens loaded in axial tension was conducted to investigate the structural behaviour, focusing on the crack formation in the serviceability limit state. As mentioned above, these straight elements are a strong simplification of the actual structural performance of circular water tanks. A total of five tensile specimens, either fully sprayed or 3D printed and sprayed with different printing patterns and reinforcement diameters were produced and tested.

These tests should serve as a preliminary study to investigate the feasibility from a structural perspective and focus on serviceability requirements. Therefore, the experiments were monitored with digital image correlation on both sides of the specimen to allow high-precision measurements of the crack kinematics and deformations.

For applicability in the construction industry, the mechanical behaviour needs to be predictable by existing models such as EN 1992–1 and EN 1992–3 [17,18], the *fib* Model Code 2010 [19] and the tension chord model (TCM) [20,21]. Therefore, the results from the experimental campaign are compared to these models. The insights gained from this experimental campaign are not limited to water tanks but help to foster the understanding of post-installed reinforcement for unreinforced concrete shells.

3. Materials and methods

3.1. Overview

The basis for the design of the specimens was a typical water tank with a diameter of 10 m and a height of 4 m (Fig. 1b). A manufacturer of concrete water tanks provided a typical conventional reinforcement layout for such a tank. The wall thickness was 225 mm with two layers of reinforcement meshes. The lower and decisive part of the wall showed a circumferential reinforcement content of 1540 mm^2/m. The same reinforcement cross-sectional area could be reached by one layer of Ø14 mm spaced every 100 mm (see Fig. 1c). Therefore, this reinforcement arrangement was chosen for the experimental campaign. A reinforcing bar diameter of Ø22 mm was also investigated to simulate larger water tanks. The specimens had to be large enough to obtain representative results while still fitting the capacity of the testing machine. The nominal dimensions were set with a length of 2000 mm of the concrete element and 3000 mm of the reinforcing bars in the direction of the tensile load. The width was 400 mm, and the total thickness was 150 mm. For the specimens with a 3D printed and a sprayed part, the printed shell was 60 mm, and the sprayed concrete was 90 mm thick. Two printing patterns were explored: (i) Two straight filaments next to each other and (ii) wavy filaments with overlapping layers. Each specimen had two orthogonal layers of reinforcement. The main reinforcement consisted of four reinforcing bars with a diameter of Ø14 mm or Ø22 mm. The distance from the edge of the specimens to the centre of the reinforcing bar was 40 mm. The secondary reinforcement was spaced every 100 mm with a diameter of Ø10 mm or Ø16 mm. Fig. 2 shows the nominal dimensions and reinforcement layout of the specimens. An overview of the testing matrix is given in Table 1.

For the 3D printed specimens, the shells with the two different patterns were printed first. Subsequently, the preassembled reinforcement

Table 1
Overview of the specimens.

Nomenclature	Inner shell	Outer shell	Interface	Main reinforcement	Secondary reinforcement
14-sprayed	Sprayed in formwork		–	4x Ø14	Ø10@100
14-3Dp-straight	3Dp	Sprayed	Straight	4x Ø14	Ø10@100
14-3Dp-rough	3Dp	Sprayed	Rough	4x Ø14	Ø10@100
22-3Dp-straight	3Dp	Sprayed	Straight	4x Ø22	Ø16@100
22-3Dp-rough	3Dp	Sprayed	Rough	4x Ø22	Ø16@100

Table 2
Material properties of the two concretes. (Abbreviations: f_c: compressive strength, f_{ct}: tensile strength, E_c: Young's Modulus, CoV: coefficient of variation).

	f_c [MPa] (CoV)	f_{ct} [MPa] (CoV)	E_c [GPa] (CoV)
3D printing	49.7 (6 %)	2.3 (10 %)	25.9 (4 %)
Spraying	46.1 (6 %)	2.2 (14 %)	25.4 (2 %)

cage was placed, fastened in front of the printed shell, and sprayed. One specimen was fully sprayed inside a formwork. After hardening, the specimens were cut to the correct dimensions and tested in a tensile test by pulling on the main reinforcing bars. Both sides of each specimen were tracked with digital image correlation to enable full-field displacement measurements during testing. These measurements were post-processed to determine the crack kinematics with the Automated Crack Detection and Measurement (ACDM) method [22,23]. In the following, the materials and methods are explained in more detail.

3.2. Materials

For the production of the specimens, conventional reinforcing steel B500B and two types of concrete were used. The 3D printing mortar was a customised mixture developed at ETH Zurich at the Chair of Physical Chemistry and Building Materials in collaboration with Knauf Gips KG and BASF. The base mixture consisted of quartz sand of varying grades, limestone filler, cement (CEM I 52.5R), fine ground gypsum, superplasticizer, stabilizer and water. The thickener and accelerator pastes were added to the base mixture during printing to enhance stability in filament shape and strength buildup, respectively. The accelerator was a calcium aluminate cement and anhydrite paste with an added stabilizer and retarder, while the thickener was a solution of sodium metasilicate and starch ether. The maximum aggregate size of the mortar was 1.2 mm. For the spraying, commercially available mortar with a maximum aggregate size of 2 mm was used. Strictly speaking, both mixes of this project are mortars since their maximum aggregate size is below 4 mm. However, for consistency, the term concrete is used throughout this manuscript.

The material characterisation of the concrete in its hardened state was conducted at the age of testing. The compressive strength f_c and Young's modulus E_c were tested on cylinders with a height of 300 mm and a diameter of 150 mm. The tensile strength f_{ct} was determined by double punch tests [24,25] on cylinders with a height and diameter of 150 mm. The results and coefficient of variation (CoV) for four samples per mix are compiled in Table 2. It can be seen that the material properties of the two concretes matched well: The 3D printing concrete was 8 % and 1 % stronger in compression and tension, respectively, and 2 % stiffer.

The reinforcement used in this study was conventional reinforcing steel of type B500B with threads at each end for anchorage. The stress–strain response of the two main reinforcements (i.e. Ø14 mm and Ø 22 mm) and the characteristic dynamic values are shown in Fig. 3. For each diameter, at least three samples were tested.

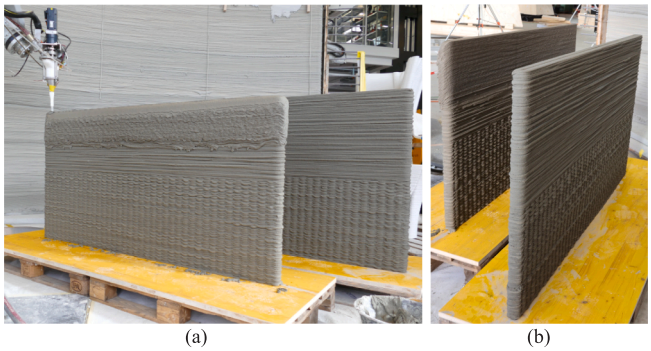

Fig. 4. 3D concrete printing of the two shells with different patterns: (a) Printing of the second shell; (b) finished shells.

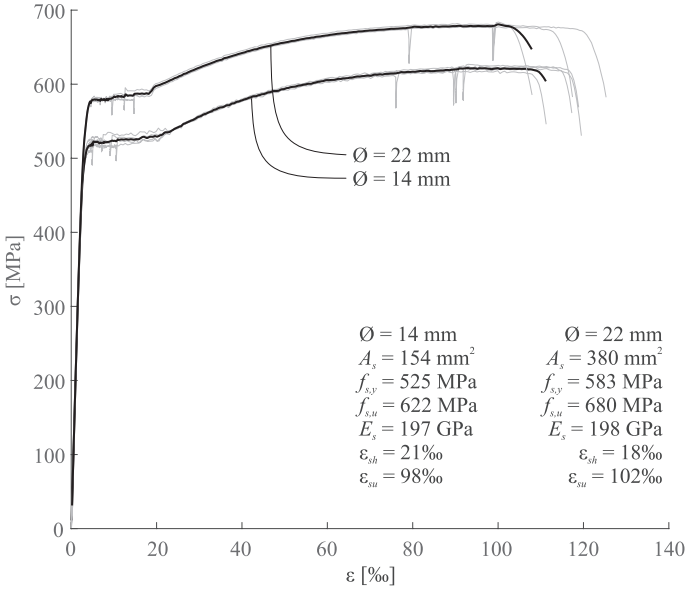

Fig. 3. Stress–strain relationship and characteristic dynamic values of the two reinforcement types used in this study. The grey curves show all tested samples, while the black curves are the average. (Abbreviations: A_s: cross-sectional area, f_{sy}: yield strength, f_{su}: ultimate strength, E_s: Young's Modulus, ε_{sh}: hardening strain, ε_{su}: ultimate strain).

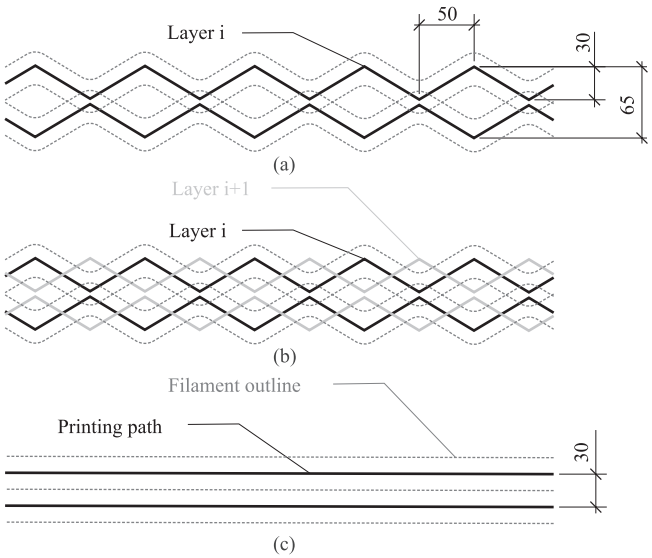

Fig. 5. Section of 500 mm of the printing path and filament outlines of the two patterns (dimensions in [mm]): (a), (b) printing path and outline of one layer, and offset between subsequent layers of the rough pattern; (c) printing path for the straight pattern.

3.3. Production

3.3.1. 3D concrete printing

The first part of the production consisted of 3D printing two shells. The basis of the printing system was an ABB robot arm. The customised extruder had a mixing chamber right before the nozzle. The dry material was mixed with the water in a continuous mixer and transported by a pump to the nozzle. At the nozzle, accelerator and thickener were added to the concrete and mixed inside the nozzle. A schematic representation of the printing setup can be found in [16].

Each shell was printed with two different patterns up to a total height of 1100 mm and a width of 2000 mm. The production process and the finished shells can be seen in Fig. 4. The pumping rate was set to 800 ml/min with an accelerator dosage of 70 ml/min and a thickener dosage of 7 ml/min. With a printing speed of 90 mm/s and a layer height of 5 mm, a filament width of approximately 30 mm was achieved. The printing speed was slightly varied to ensure good printing quality, with a time interval between consecutive layers of around 40 s. The total printing time for one shell was approximately 2 h. Due to technical problems, the thickener pump needed to be stopped in the upper part of the second shell. The resulting reduced printing quality can be seen in Fig. 4a. However, Fig. 4b shows that the printing defects were limited to one side. Therefore, the element could still be used.

The lower pattern had a wavy geometry to increase the roughness (in the following, referred to as *rough pattern*). The upper part was produced with two straight filaments (*straight pattern*). A section of the printing paths and filament outlines of the patterns are shown in Fig. 5. In the rough pattern, the nozzle was oscillating 30 mm over a length of 100 mm (Fig. 5a). Each layer was shifted by 50 mm to the one above or below. Straight lines with a distance of 30 mm produced the straight pattern.

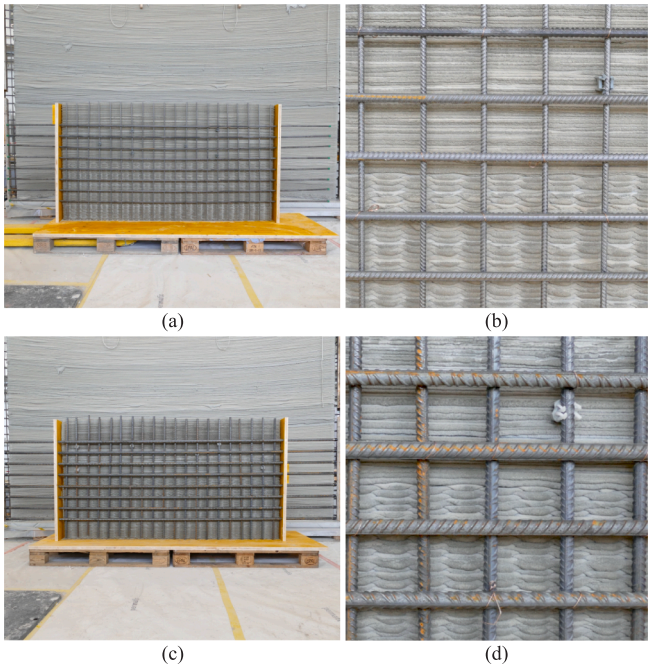

Fig. 6. Reinforcing arrangement for the two 3D printed shells: (a) and (c) view of the arrangement of the main reinforcement of Ø14 mm and Ø22 mm, respectively; (b) and (d) close-up view with the two different printing patterns behind the reinforcement cages with Ø14 mm and Ø22 mm main reinforcement, respectively.

3.3.1.1. Reinforcement placement. After the production of the two shells, the reinforcement meshes were added the next day. The meshes were preassembled and held by timber scaffolding, serving as stop formwork for the sprayed concrete and, at the same time, ensuring stability and the correct concrete cover. The resulting setup is illustrated in Fig. 6. Conventional spacers were placed between the shell and the reinforcement, measuring 30 mm for the Ø14 mm configuration and 20 mm for the Ø22 mm configuration. These spacers were used to ensure that the sprayed concrete covered the full circumference of the reinforcing bars to achieve good bond between the reinforcement and the sprayed concrete.

3.3.1.2. Spraying. After the reinforcement placement, the two shells were housed in a tent for spraying. The spraying was performed manually two days after printing. In addition to the two 3D printed shells, one specimen was sprayed inside a conventional formwork without additional vibration nor compaction. Fig. 7 gives an overview of the spraying process. Before concrete spraying, the printed surfaces were sprayed with water to improve the interface behaviour. Subsequently, the concrete was sprayed in multiple layers (Fig. 7a). Once the height of the reinforcement was reached, the sprayed concrete was flattened with a trowel (Fig. 7b). After the desired spraying thickness was reached, the surface was smoothened. The specimens were afterwards covered with a plastic foil and left to cure until they were cut.

3.3.1.3. Cutting. Two weeks after printing, the specimens were cut to the correct width. The resulting surfaces are shown in Fig. 8. The cut surfaces show the secondary reinforcement, the printing and spraying quality, and the interface. For the straight printing (i.e. 14-3Dp-straight), a small gap between the printed filaments was visible. For the rough pattern, no such gaps occurred. The width of the printed parts was around 70 mm for the straight pattern and ranged from 70 to 80 mm for the rough pattern. The sprayed concrete appeared to embed the reinforcement well. However, large air entrapments were visible in the sprayed concrete. These air entrapments largely depend on the operator, especially for closely spaced reinforcement [26]. They are not expected to influence the structural performance. However, they should be considered for water permeability.

3.4. Specimen geometry

After cutting, the printed specimens were scanned with a laser scanner of the type Leica RTC360 with an accuracy of 1.5 mm. The

Fig. 7. Spraying process: (a) application of the first spraying layer; (b) compaction of the sprayed concrete at the height of the reinforcing bars; (c) spraying inside the formwork of Specimen 14-sprayed.

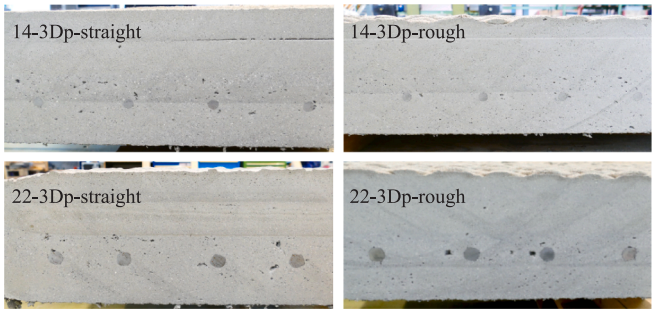

Fig. 8. Side view of the cut surface of the four printed specimens.

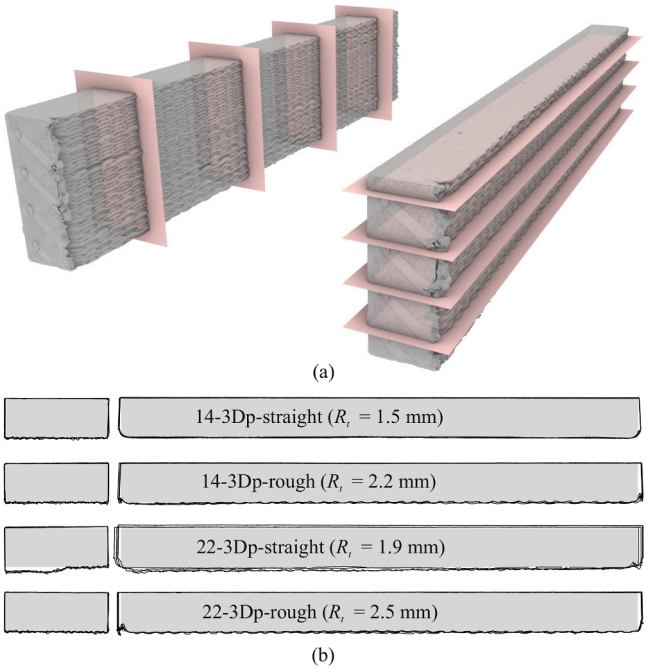

Fig. 9. Scanning of the specimens: (a) four representative sections through the scan of Specimen 22-3Dp-rough; (b) resulting sections (black curves) and the nominal geometry (grey area) for all 3D printed specimens. (Abbreviation: R_t: peak-to-mean roughness).

resulting digital models provided quality control of the fabrication process. In Fig. 9, four vertical and horizontal sections of each 3D printed specimen are recorded. The sections are spaced every 500 and 100 mm, respectively. Except for the part of the specimen 22-3Dp-straight without thickener (see Section 3.3.1), the outlines of the scanned samples matched the nominal dimensions well.

The roughness of the specimens was measured with the sand patch test [19,27] on the outside surface. For the Specimen 22-3Dp-straight, only the part printed with added thickener was considered since the texture of the part without thickener was different on the outside than

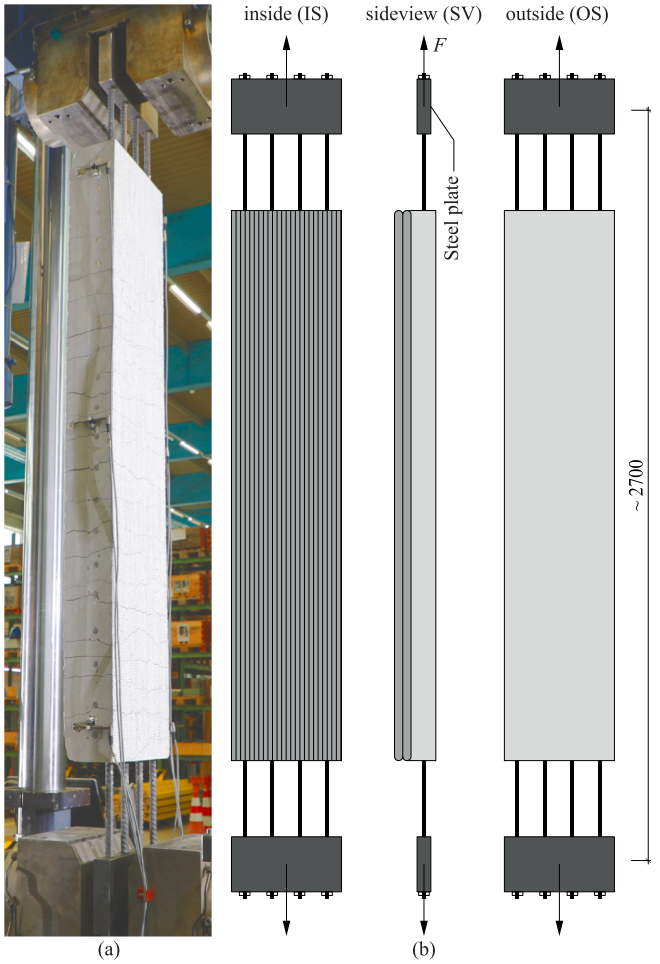

Fig. 10. Loading setup: (a) Image of a specimen during loading; (b) schematic representation of the inside, side view and outside of a specimen under loading.

Table 3
Overview of the digital image correlation parameters.

Cameras	Resolution [Mpx]	Focal length [mm]	Baseline [mm]	Stereo angle [°]	Resolution [px/mm]	Field of view [mm × mm]	Subset size [px]	Step size [px]
FLIR	12.3	25	1376	19.8	2.0	2231 × 1634	25	6
ProSilica	29	28	636	20.2	3.0	2576 × 1718	19	5

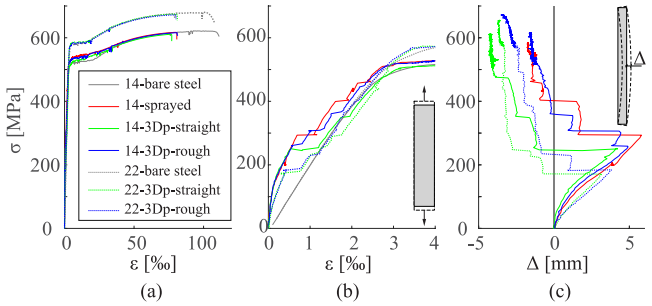

Fig. 11. Overview of all samples: (a) stress–strain relationship of all specimens; (b) stress–strain in the cracked-elastic phase; (c) out-of-plane deformations of the centre point.

on the inside. For the measurement, a volume of 50 ml of fine-grained sand was spread over the surface until a flat circle was reached. From the resulting diameter, the "peak-to-mean" roughness R_t [19] could be calculated by dividing the volume by the circle area. The R_t for the 3D printed specimens are shown in Fig. 9. According to the *fib* Model Code 2010, all surfaces fall in the category of "rough" (≥1.5 mm). As expected, the roughness is increased for the patterns with the rough pattern compared to the straight pattern.

3.5. Testing setup, instrumentation and measurement

For testing, the specimens were vertically placed in a universal testing machine with a maximum loading capacity of 1600 kN. The reinforcing bars were anchored with steel plates with a height of 200 mm, a width of 400 mm and a thickness of 50 mm (see Fig. 10). The total load F was applied with a speed of 0.1 mm/s up to the onset of hardening of the reinforcement, and the speed was increased to 0.3 mm/s afterwards. The first specimen (i.e. 14-sprayed) was loaded with a constant speed of 0.15 mm/s. The specimens were tensioned until failure, and the stresses in the reinforcement were determined by dividing the applied tensile load by the nominal cross-sectional area of the main reinforcement.

Both sides of the specimens were tracked with full-field digital image correlation during testing. For this measurement technique, black speckles on a white surface were needed. On the smooth surface, this speckling was applied with rollers; for uneven (i.e. printed) surfaces, the speckling was produced by flicking a brush. The smooth (i.e. sprayed) surface was tracked by two FLIR Grasshopper3 12.3 Mpx monochrome cameras with Quioptic MeVis-C 1.6/25 lenses and the other side with two ProSilica GT6600 29 Mpx monochrome cameras with Zeiss Distagon T* 2/28 lenses. The measurement frequency was 1 Hz. The post-processing was done with the commercial software VIC 3D by Correlated Solutions [28]. Table 3 gives an overview of the parameters of each camera system.

This setup allowed tracking full-field three-dimensional deformations of the surface of the specimens. The surface strains were

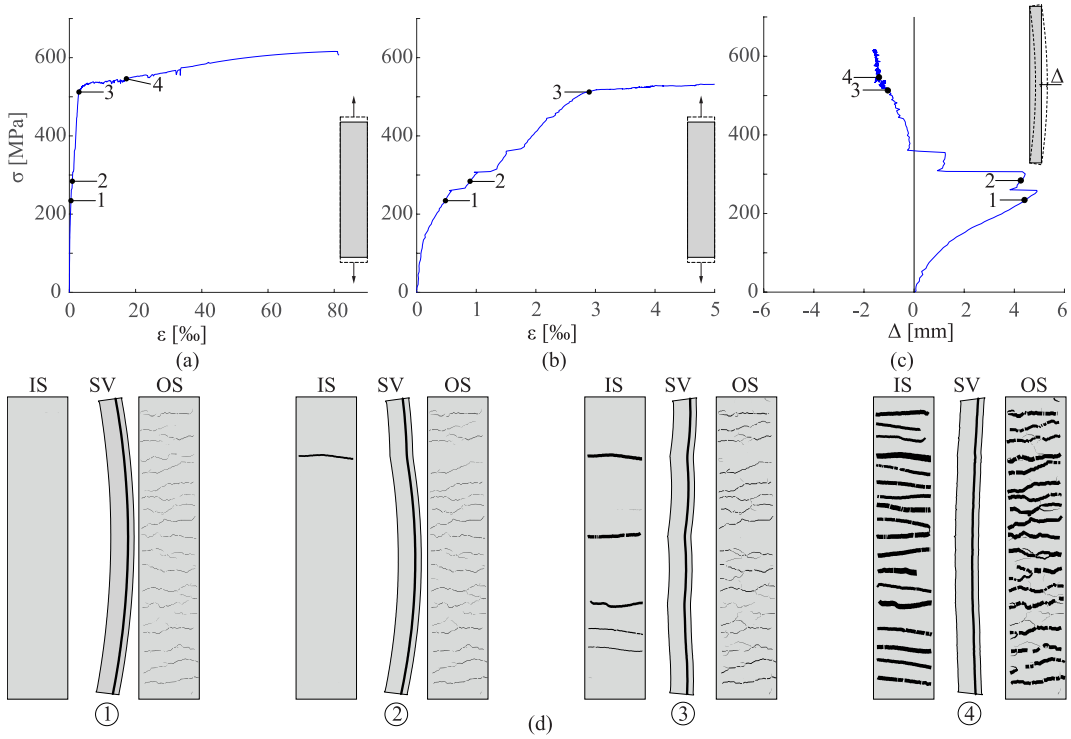

Fig. 12. Load-deformation behaviour and crack formation and kinematics for Specimen 14-3Dp-rough: (a) stress–strain relationship; (b) stress–strain in the cracked-elastic phase; (c) out-of-plane deformations of the centre point; (d) inside (IS), side (SV) and outside (OS) view of the specimen at four characteristic load levels with the crack opening shown on the inside and outside and the deformation in the side view exaggerated by a factor of 20.

determined from these measurements by virtual extensometers in the inner 1.2 m of the specimens. The crack formations and kinematics were measured with the ACDM method [22,23]. This post-processing method allowed a visual representation of the cracks and precise measurement of the crack openings. For the crack openings versus stress diagrams, the average crack opening at the surface of the specimen was computed and plotted.

4. Results

4.1. Load-deformation behaviour

Fig. 11 shows the load-deformation behaviour of all tested specimens. The global behaviour of all specimens was similar, with the first cracks forming on the outside, i.e., the side of the reinforcement. During the cracked-elastic phase, all specimens initially exhibited tension stiffening accompanied by out-of-plane deformations in the direction of the reinforcement,i.e., towards the outside, amounting up to 5.7 mm (14-sprayed). At a threshold of approximately 250 MPa and 170 MPa for the specimens with Ø14 mm and Ø 22 mm, respectively, out-of-plane deformations reverted abruptly due to crack formations on the inside (see below). This realignment led to a step-wise increase in the strains at constant stresses (see Fig. 11b). Afterwards, all specimens exhibited slight out-of-plane deformations towards the inside. Upon further increasing the applied load, yielding of the reinforcement was reached. For the specimens with Ø14 mm, the stresses at yielding were significantly higher than for the bare reinforcing bars. In contrast, the specimens with Ø22 mm closely followed the stress–strain relationship of the bare bar. After the onset of hardening, all specimens showed a similar behaviour as the bare reinforcing bar and failed at a load close to the ultimate strength of the bare reinforcing bars, at average strains of around 80 ‰. In the following, the crack formation, as the decisive factor for the serviceability of water tanks, is examined in more detail.

Fig. 12 displays the load-deformation behaviour and the crack formation of the Specimen 14-3Dp-rough. Four characteristic load levels were chosen: (Level 1) close to the maximum out-of-plane deformations, (Level 2) after the first crack on the inside, (Level 3) at the onset of yielding and (Level 4) at the beginning of the hardening. The same figures for all other specimens are compiled in Appendix A.

In the first phase up to Level 1, the out-of-plane deformations towards the outside increased and closely spaced cracks formed on the outside of the specimen. The curvature along the specimen was fairly constant, and the inside was under compression; therefore, no cracks formed. Upon the first “snapback” (Level 2), the out-of-plane deformations were reduced and a first wide crack formed on the inside. With the opening of this crack on the inside, the crack at the same height on the outside closed. With increasing load up to Level 3, this phenomenon repeated itself, with multiple new cracks forming on the inside and closing of the respective cracks on the outside until the specimen was straightened and out-of-plane deformations occurred towards the inside. During yielding of the reinforcement (from Level 3 to 4), the cracks on both sides homogenised with the same amount of cracks opening on the inside and outside. Even more than the crack formation in relation to the load-deformation behaviour, the actual crack openings are essential for the serviceability of water tanks. Therefore, the following section presents and discusses the crack opening versus stresses for all specimens.

4.2. Crack kinematics

The opening of the cracks in the central 1.2 m of each specimen is recorded in Fig. 13. Only stresses up to the onset of yielding are considered here since this part is decisive for serviceability. The three specimens with the main reinforcement of Ø14 mm exhibited similar crack opening behaviour independent of the fabrication method. After a stiff initial phase, the cracks on the outside opened linearly, with the widest cracks opening up to 0.4 mm. A few cracks on the outside closed suddenly with a simultaneous large opening of cracks on the inside. These cracks correspond to the behaviour described in the section above. With the opening of the cracks on the inside, the corresponding cracks

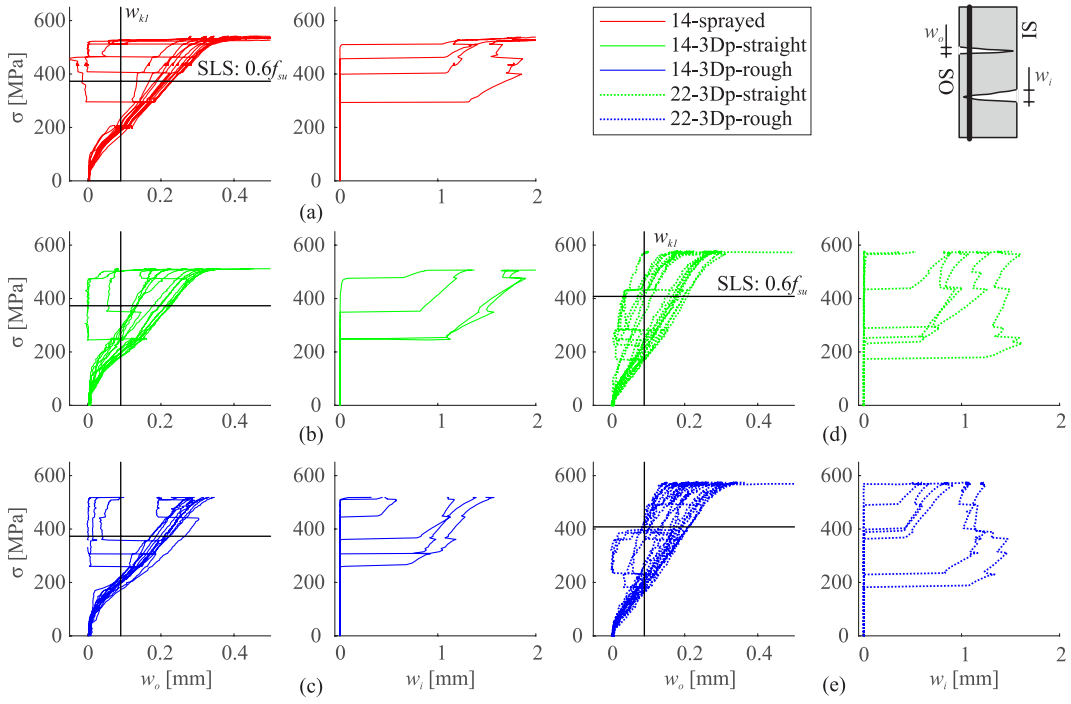

Fig. 13. Crack opening versus stresses of all specimens for cracks on the inside and outside: (a) 14-sprayed; (b) 14-3Dp-straight; (c) 14-3Dp-rough; (d) 22-3Dp-straight; (e) 22-3Dp-rough. (Abbreviations: w_o: crack opening on the outside, w_i: crack opening on the inside, w_{k1}: crack limited for Tightness Class 1, SLS: serviceability limit state).

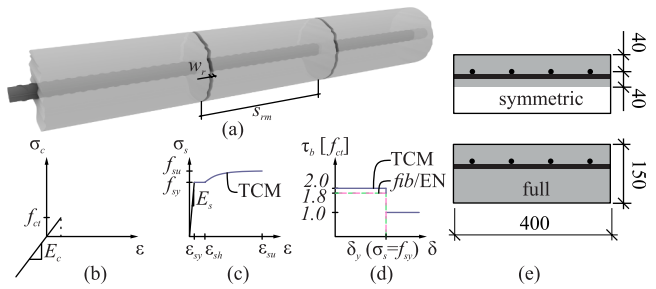

Fig. 14. Cracked reinforced concrete under uniaxial tension: (a) schematic representation of a cracked reinforced concrete element; (b) behaviour of the concrete; (c) material behaviour of the bare reinforcing steel; (d) bond strength model; (e) considered cross-sectional areas (dimensions in [mm]). (Abbreviations: TCM: tension chord model, EN: EN 1992–1, *fib*: *fib* Model Code 2010).

on the outside closed fully or remained slightly open due to the reversal of out-of-plane deformations. The cracks on the inside opened by more than 1 mm. The higher the load at which the inside cracks opened, the lower their initial opening. The behaviour was similar for the specimens with the larger main reinforcement Ø22 mm. However, more cracks formed on the inside. The crack spacing was calculated from the cracked elements once cracks had formed on both sides, i.e. Level 4 in Fig. 12. The average crack spacing for the specimens with Ø14 mm and Ø22 mm was 104 mm and 95 mm, respectively.

The tensile load acting in the serviceability limit state can reasonably be assumed to be at 60 % of f_{su}. According to EN 1992-3 [18], the maximum allowed crack opening for Tightness Class 1 w_{k1} for a water tank with a height of 4 m and a wall thickness of 0.15 m is 0.09 mm. In Fig. 13, the threshold of the serviceability limit state and w_{k1} are shown for the cracks on the outside. All cracks, except the ones that closed due to a crack opening on the inside, infringe this limit. However, since the cracks are recorded on the surface and only occur on the outside, this behaviour needs further examination (see Section 6).

5. Comparison to existing models

5.1. Model overview

For the prediction of the load-deformation behaviour and crack opening, three different models were considered: EN 1992-1 [17], the *fib* Model Code 2010 [19] and the TCM [20,21]. These models were chosen since they all follow the same underlying principles: after concrete cracking, the composite action of a tensile member is composed of the stress–strain behaviour of the bare steel, whose strains are reduced by the concrete tensile contribution between cracks (i.e. tension stiffening effect). It should be noted that the assumptions of code provisions (i.e. EN 1992–1 and *fib* Model Code 2010) generally are more conservative than the TCM to increase the safety margin. However, since they are based on the same principles, they are directly compared in this study.

For each model, the predictions were calculated based on two approaches. In the first approach, the entire nominal cross-section of the specimens was considered, and the eccentricity of the reinforcing bars was neglected. In the second approach, only the concrete area symmetric with respect to the main reinforcement layer (i.e. twice the cover to bar axis distance of 40 mm), from here on referred to as *symmetric cross-section*, was considered. Fig. 14 shows a schematic representation of a cracked reinforced concrete element under uniaxial tension, the material properties and the cross-sections considered. In the following, each model and its assumptions are introduced.

The crack opening w_r is the product of the mean crack spacing s_{rm} and the difference between the mean strain of the reinforcement ε_{sm} and the concrete ε_{cm} over this distance, i.e.:

$$w_r = s_{rm}(\varepsilon_{sm} - \varepsilon_{cm}) \tag{1}$$

In EN 1992–1 [17], the difference in mean strains is given as,

$$\varepsilon_{sm} - \varepsilon_{cm} = \frac{\sigma_{sr} - k_t \frac{f_{ct,eff}}{\rho_s}(1 + \alpha_e \cdot \rho_s)}{E_s} \geq 0.6\,\frac{\sigma_{sr}}{E_s} \tag{2}$$

with σ_{sr} being the stress in the reinforcement, k_t a factor for the duration of loading (k_t set as 0.6 for short them loading), $f_{ct,eff}$ the effective tensile strength of the concrete, ρ_s the reinforcement ratio and α_e the ratio between the Young's Modulus of the concrete E_c and steel E_s. The minimum difference of the mean strains is limited to 60 % of the bare steel strains. The maximum crack spacing is calculated with the four factors k_1 to k_4, the concrete cover c and the ratio between the reinforcing bar diameter Ø and the reinforcement ratio ρ_s:

$$s_{r,max} = k_3 c + k_1 k_2 k_4 \frac{\varnothing}{\rho_s}\left(\leq \frac{\sigma_{sr} \cdot \varnothing}{3.6 f_{ct,eff}}\ (NA)\right) \tag{3}$$

For the values of k_1 to k_4, the German National Annex (NA) was considered. In the German NA, the product of k_1 and k_2 is 1.0, $k_3 = 0$ (i.e., no consideration of the concrete cover), and $k_4 = 1/3.6$. A discussion on the values proposed by EN 1992-1 without NA can be found in Section 6.

The *fib* Model Code 2010 [19] uses the same formula for the difference in mean strains as EN 1992–1. However, instead of k_t, the factor β is used, no limitation is set, and for the tensile strength of the concrete, the mean tensile strength f_{ctm} is considered instead of $f_{ct,eff}$. For this study, the average experimental tensile strength of the sprayed concrete will be used for f_{ctm} and $f_{ct,eff}$. The maximum crack spacing for short-term loading and stabilised cracking stage is:

$$s_{r,max} = 2 \cdot k \cdot c + \frac{1}{3.6}\frac{\varnothing}{\rho_{s,eff}} \tag{4}$$

The factor k for considering the concrete cover is 1.0. Therefore, the only difference between the *fib* Model Code 2010 and EN 1992-1, considering the German NA, is the increase of the maximum crack spacing by twice the concrete cover. In both models, the bond strength between the reinforcing bar and the surrounding concrete τ_{b0} is 1.8 f_{ct}.

The crack spacing for calculating the crack opening is $s_{r,\max}$ for both codes. In the TCM, on the other hand, the crack spacing is varied by a factor λ ranging from 0.5 for the minimum theoretical crack spacing $s_{r,\min}$ to 1.0 for its maximum theoretical value $s_{r,\max}$. The bond strength is set as 2.0 f_{ct} before yielding and $\tau_{b1} = f_{ct}$ after the onset of yielding. The mean strains of the reinforcing bar are:

$$\varepsilon_{sm} = \frac{\sigma_{sr}}{E_s} - \frac{\lambda \cdot f_{ctm}(1 - \rho_s)}{2 \cdot \rho_s \cdot E_s} \tag{5}$$

With the elongation of the concrete

$$\varepsilon_{cm} = \frac{\lambda \cdot f_{ctm}}{2 \cdot E_c} \tag{6}$$

and the maximum crack spacing

$$s_{r0} = \frac{\varnothing \cdot f_{ctm} \cdot (1 - \rho_s)}{2 \cdot \tau_{b0} \cdot \rho_s} = \frac{\varnothing}{4}\left(\frac{1}{\rho_s} - 1\right) \tag{7}$$

the crack opening can be expressed as:

$$w_r = \frac{\lambda \cdot s_{r0}\,(2\sigma_{sr} - \lambda \sigma_{sr0})}{2 \cdot E_s} \tag{8}$$

where σ_{sr0} is the stress in the reinforcement at cracking.

In EN 1992-1 and the *fib* Model Code 2010, the material behaviour of the bare reinforcing steel is assumed to be linear-elastic, and the equations are only defined up to the yield strength. In contrast, the dissertation of Alvarez [20] extends the TCM for reinforcing steel with a yield plateau and strain hardening. The model relies on the yield f_{sy} and

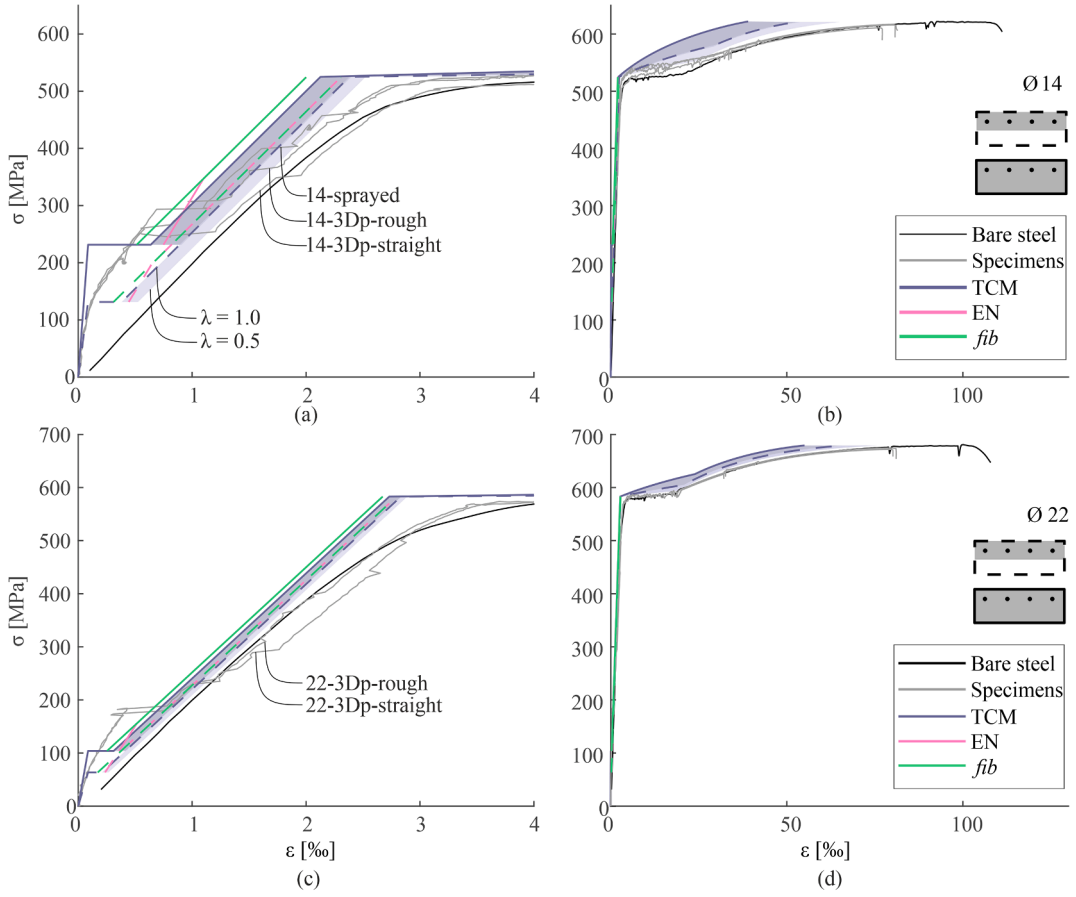

Fig. 15. Comparison between the experiments and the prediction models of the stress–strain behaviour: (a) and (c) cracked elastic behaviour of Ø14 and 22 mm; (b) and (d) stress–strain behaviour of Ø14 and 22 mm. The full lines of the models show the results for the full cross-section, and the dashed ones show the results for the symmetric cross-section, both for $\lambda = 1$. The blue coloured areas depict the range of λ from 0.5 to 1. (Abbreviations: TCM: tension chord model, EN: EN 1992–1 (NA), *fib*: *fib* Model Code 2010). (For interpretation of the references to colour in this figure legend, the reader is referred to the web version of this article.)

ultimate strength f_{su}, the yield ε_{sy}, hardening ε_{sh} and ultimate strain ε_{su}, and three fitting parameters k_a, k_b and k_c. For the two main reinforcements, the material parameters from the experimental study were taken. The parameters and details of the material model are summarised in Appendix B.

5.2. Load-deformation behaviour

Fig. 15 compares the experiments and the model predictions for the symmetric and full cross-section. For the models, ε_{sm} is plotted. Therefore, the mean strain in the concrete (see Eq. (6)) was added to the difference in mean strains. The blue areas in the graphs represent the range in the TCM by varying λ from minimum to maximum theoretical crack spacing, i.e., from 0.5 to 1.0. Considering the full cross-section (continuous lines) reduces the mean strains in the reinforcement compared to the symmetric cross-section (dashed lines) due to increased tension stiffening. In the cracked-elastic state, the three models show similar stress–strain responses, with the largest tension stiffening being calculated for the *fib* Model Code 2010. Before forming the first cracks on the inside, i.e. below 250 and 170 MPa for Ø14 mm and Ø22 mm, respectively, the models underestimate the stresses for given strains. However, before reaching yielding of the reinforcement, the stresses are overestimated. The smooth transition from the cracked-elastic state to the yield plateau shown by the specimens is not reflected well by the models. After yielding, the TCM overestimates the stresses for given strains and the strain at failure is underestimated for all configurations. The closest ultimate strain was achieved with the TCM with the symmetric cross-section for $\lambda = 0.5$. In addition to predicting the global load-deformation behaviour, the crack widths are analysed in the following section.

5.3. Crack kinematics

Fig. 16 shows the comparison between the models and the cracks of all specimens. Again, the lines are drawn for the maximum crack spacing resulting from the symmetric (dashed lines) or full cross-section (continuous lines), and the blue areas indicate the range achieved by varying the parameter λ. For the cracks forming on the inside (Fig. 16b and d), the models cannot predict the behaviour since the opening of these cracks was not controlled by reinforcement but opened suddenly due to the realignment of the specimens. On the outside of the specimen, the crack formation (Fig. 16a and c) was controlled by the reinforcement. It can be seen that the TCM with the higher bond predicted the smallest openings. By reducing bond stresses for the calculation of the crack spacing from 2 f_{ct} to 1.8 f_{ct} (EN 1992–1), the crack opening increases, and by adding the concrete cover for the crack spacing (*fib* Model Code 2010), the widest openings are predicted. The closest fit is reached for the symmetric cross-section, and the cracks lie in the range of the TCM with symmetric cross-section for λ from 0.5 to 1.0. While the TCM gives the best predictions for the actual behaviour, applying the EN 1992–1 and *fib* Model Code 2010 ensures a safe design of the crack opening.

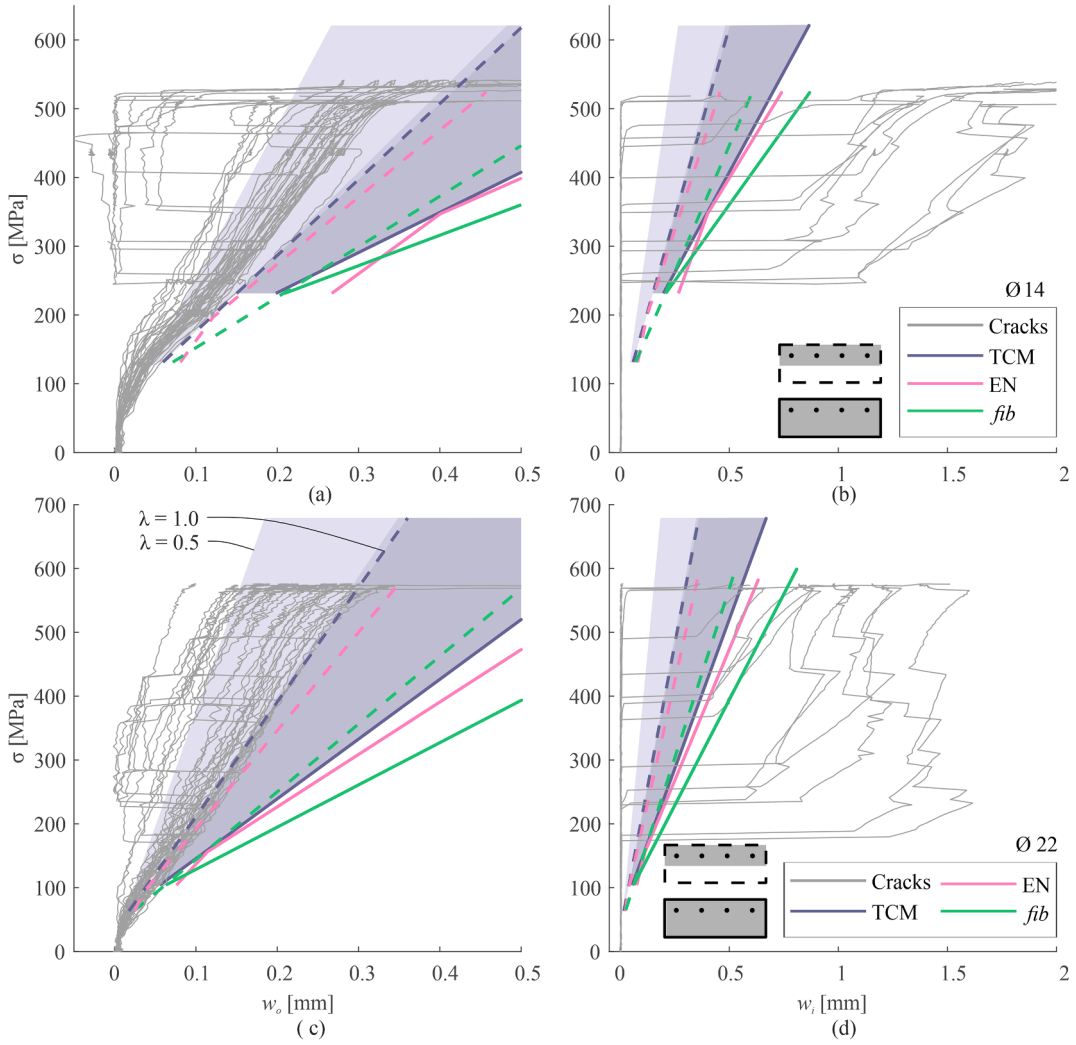

Fig. 16. Prediction of the crack opening and comparison to the experimental measurements: (a) and (c) cracked opening on the inside of Ø14 mm and Ø22 mm; (b) and (d) crack opening on the outside of Ø14 mm and Ø22 mm. The full lines of the models show the results for the full cross-section, and the dashed ones show the results for the symmetric cross-section, both for λ = 1. The blue coloured areas depict the range of λ from 0.5 to 1. (Abbreviations: TCM: tension chord model, EN: EN 1992–1 (NA), *fib*: *fib* Model Code 2010). (For interpretation of the references to colour in this figure legend, the reader is referred to the web version of this article.)

6. Discussion

The load-deformation behaviour of all specimens with the same main reinforcement was similar, indicating that the production with a 3D printed shell does not influence the structural behaviour. The eccentric reinforcement was the main difference from conventional tank wall cross-sections. Under uniaxial tension, the specimens showed out-of-plane deformations followed by realignment resulting in small controlled cracks on the outside and sudden wide cracks on the inside. This behaviour was caused by the eccentricity of the reinforcement resulting in a bending moment acting on the specimen. In the initial state of the specimen, cracks only appeared on the outside, and the curvature caused by the bending was fairly constant over the entire length of the specimen, causing large out-of-plane deformations. Once cracks formed on the inside, the specimens realigned below the load up to the fully cracked state. However, since there was no reinforcement controlling the crack opening on the inside, these cracks opened suddenly with initially large spacings and openings. The rotation caused by each wide crack on the inside compensated for several narrow cracks on the outside. Due to this sudden and uncontrolled correction, the specimens overshot the realignment and exhibited deformations towards the inside. The larger reinforcing bar diameter seems to have reduced the

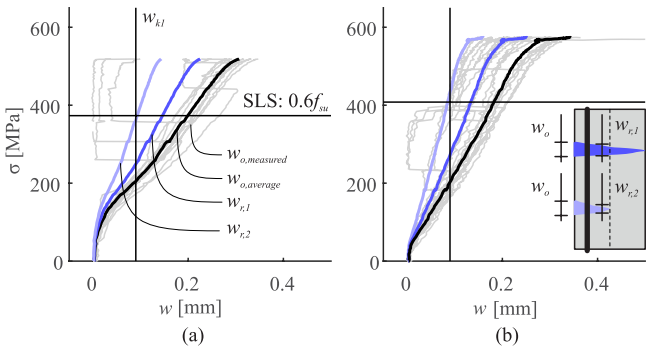

Fig. 17. Effective crack opening: (a) Specimen 14-3Dp-rough; (b) Specimen 22-3Dp-rough. (Abbreviations: $w_{o,measured}$: Crack opening measured on the surface, $w_{o,average}$: Average measured crack opening of cracks without sudden reduction of the opening, $w_{r,1}$: Effective crack opening at the height of the reinforcement for a crack through the specimen, $w_{r,2}$: Effective crack opening at the height of the reinforcement for a crack trough half the specimen.).

deformations towards the outside. However, the deformations towards the inside were the same or even more pronounced compared to the smaller reinforcing bar diameters. The higher stiffness of the larger reinforcing bars might have limited the out-of-plane deformations towards the outside. Since no reinforcement was provided on the inside, the deformations towards this side were similar.

The experimental crack openings exceeded the threshold stipulated by EN 1992–3. However, the crack openings only occurred on one side. If a crack does not propagate through the cross-section and the inside remains under compression, no leakage is expected even though the crack width exceeds the limit. Furthermore, the crack openings were measured on the surface, and the actual crack opening at the level of the reinforcement, depending on how far the crack extended towards the inside, was smaller. Fig. 17 shows the effective crack openings $w_{r,1}$ and $w_{r,2}$ at the level of the reinforcement, assuming that the cracks extended over the entire or half the thickness, respectively, and opened linearly over their extension. Depending on the latter, the effective crack opening decreases substantially. If the actual crack only reached half the specimen thickness, the effective crack opening at the level of the reinforcing bar would have complied with the limit proposed by EN 1992–3, i.e., 0.09 mm.

The three models applied in this study were developed for symmetrically reinforced tension chords. As expected, applying these models for the inside cracks, where no reinforcement controls the crack opening, did not give meaningful results (see Fig. 16b and d). Therefore, only the application of the models for the outside cracks is considered in the following (see Fig. 16a and c). The predictions of the models with the full cross-section show that neglecting the eccentricity gives results with a large safety margin. The overestimation of the crack opening indicates that for eccentric reinforcement, not the entire cross-section was activated. The good predictions obtained when only considering the concrete area symmetric with respect to the main reinforcement affirms the assumption that only part of the concrete was activated in tension between the cracks. The best fit was reached for the TCM with a factor λ of 0.5. This match indicates good bond (rather 2 f_{ct} than 1.8 f_{ct}) between the sprayed concrete and the reinforcing bars and that a consideration of the concrete cover for the crack spacing, as proposed by the *fib* Model Code 2010, results in more conservative predictions for the crack opening. As mentioned above, the better fit of the TCM is as expected, as the other two models are code provisions, which typically have larger safety margins. For the analysis in Section 5, the German NA was considered. In the EN 1992–1, the values for k_1 to k_4 are 0.8 for k_1 (high bond bars), 1.0 for k_2 (pure tension), 3.4 for k_3 and 0.425 for k_4, resulting in

$$s_{r,max} = 3.4 \cdot c + 0.8 \cdot 1.0 \cdot 0.425 \frac{\varnothing}{\rho_s} \tag{9}$$

The resulting crack spacing and opening would be even larger than predicted by the *fib* Model Code 2010. On the other hand, the factor k_2 in Eq. (9) could range from 0.5 (pure bending) to 1.0 (pure tension), depending on the applied strains. With the eccentricity in the presented study, a value of 0.6 would result for k_2. With this value, the last term of Eq. (9) would be smaller than for the *fib* Model Code 2010 or the TCM. However, the overestimation of the crack spacing would persist due to the large factor considering the concrete cover.

The activation of the concrete area in tension between the cracks might have also been influenced by the interface roughness and location of the reinforcement, as shown in Fig. 18. For a monolithically cast concrete element, no interface exists. On the other hand, the lowest roughness is achieved by spraying against a smooth surface. In some 3DCP applications, the surface is smoothened during printing, as shown in the middle of Fig. 18a. This approach would result in a roughness between a cast, smooth surface and a printed surface without smoothening. The two interfaces in this study are shown in Fig. 18a on the right. In the experimental campaign, no delamination could be observed. Therefore, these two interfaces appeared to transfer the stresses well. For surfaces classified as "rough" (see Section 3.4), the *fib* Model Code 2010 specifies a mean shear resistance for concrete grades ≤ C50 between 1.5 and 2.5 MPa [19]. Since this resistance is in the order of the tensile strength of the concrete, it could be expected that the force transfer between the two surfaces works well. However, since the used materials are not standardised concrete, these values should be taken with care. The influence of various parameters on the load transfer between digitally fabricated elements is currently being investigated by different authors (e.g. [29,30]). However, the hydrostatic pressure inside an actual water tank would further counteract possible delamination.

When loading a reinforcing bar in tension, forces are transferred from the reinforcement to the concrete by bond. This load transfer results in tensile stresses in the concrete (see schematically indicated green areas in Fig. 18b) [31]. Depending on the position of the reinforcement relative to the interface, these tensile stresses might extend beyond the interface, requiring the transfer of shear and tensile stresses across it. Since the experimental observations were best predicted by accounting for the symmetric part of the concrete around the reinforcement only, and the concrete cover was smaller than the distance between reinforcing bars and the interface (see Fig. 2), the tensile stresses likely did

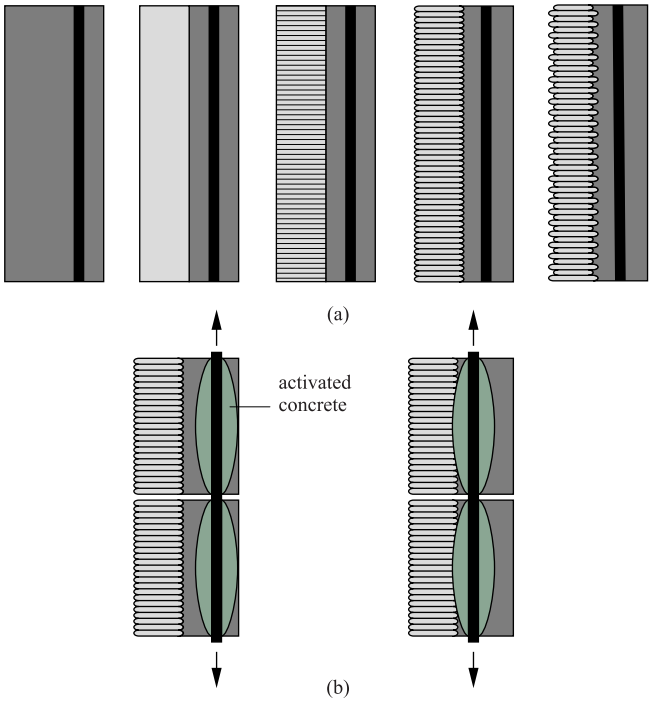

Fig. 18. Interface parameters: (a) from left to right: increasing roughness; (b) difference in the activated concrete area depending on the reinforcing bar position.

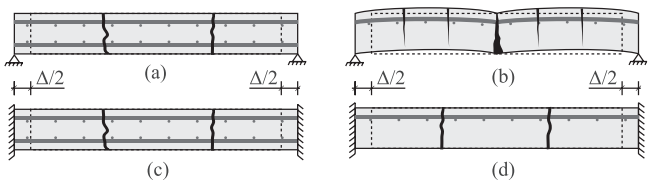

Fig. 19. Crack formation from imposed deformations Δ of a water tank wall segment (plan curvature of the wall neglected): (a) and (c) symmetrically reinforced wall segment with pin support and full rotational restraint, respectively; (b) and (d) eccentrically reinforced wall segment with pin support and full rotational restraint, respectively.

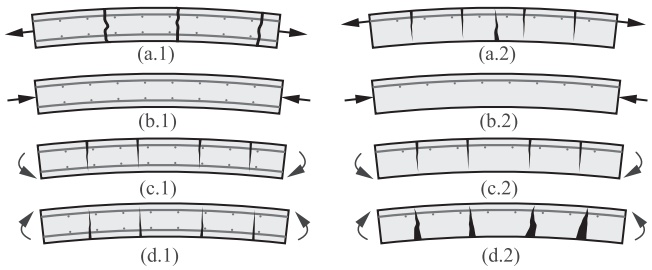

Fig. 20. Different loading configurations on a tank segment: (a) pure tension; (b) pure compression; (c) negative bending; (c) positive bending; (1) conventional reinforcement layout; (2) eccentric reinforcement layout.

not extend beyond the interface. For different geometries, however, this interface might influence the activation of the concrete by bond.

One major point to consider is whether the chosen setup is representative of the actual behaviour of a circular tank wall. In the experiments, the tension chords were pulled on the reinforcement with a free length of around 500 mm. Therefore, the setup did not provide any significant out-of-plane stiffness nor restraint. For a circular tank, however, each wall segment subjected to tensile hoop stresses is restrained in its deformations by neighbouring segments; on average, the curvatures around the vertical axis must vanish by symmetry. Otherwise, integration of the curvatures around the tank perimeter would result in a relative rotation, which cannot occur since the wall is continuous. Fig. 19 shows the presumed crack formation for symmetrically and eccentrically reinforced wall elements which are pin supported, representing the experimental setup (Fig. 19a and b) and with full rotational restraint (Fig. 19c and d) subjected to imposed horizontal deformations. For a symmetrically reinforced tank wall, the behaviour with or without rotational restraint is expected to be similar. However, as shown in this study, the out-of-plane deformations and, therefore, the boundary conditions play a decisive role in an eccentrically reinforced wall. Under loading, a tank would uniformly expand towards the outside. Therefore, it is unlikely that only the outer surface of the wall would crack first, followed by sudden cracks on the inside, as observed in the experiments. Instead, it is expected that the uniform elongation of the tank results in cracks with a constant opening over the wall thickness, just like in a symmetrically reinforced wall. The opening of these cracks will be controlled by the reinforcement.

The actual behaviour of the proposed reinforcement layout would require further experimental studies, for example, on full-scale water tanks, testing setups with restraint rotations or advanced numerical simulations, particularly regarding the part of the concrete cross-section activated in tension in the rotationally restrained situation.

So far, the only loading condition studied for the wall segment was direct tension. However, depending on the location and support conditions of the water tank, different load cases will occur. Compression forces, for example, occur in an empty cylindrical water tank homogeneously embedded into the ground. Furthermore, a partly embedded water tank would be subjected to positive and negative bending moments. Fig. 20 shows the different loading conditions and presumed crack patterns for a symmetrically and eccentrically reinforced wall segment. For compression forces, no cracks form, and the position of the reinforcement should not significantly influence the behaviour. The outside reinforcement would act as a bending reinforcement for negative bending, controlling the crack opening and ensuring structural integrity. For positive bending, on the other hand, the eccentrically reinforced wall does not provide any reinforcement in the area under tension. Therefore, this loading might lead to excessive cracking or even brittle failure. However, as discussed above, the restraint from the wall due to its closed circular shape might avoid failure by redistributing the loads. In addition to the various loading conditions in the circumferential direction of the wall, the loading over the height of the wall must be considered. Since the reinforcement arrangement is also eccentric in this vertical direction, a similar behaviour as discussed above is expected.

The presented study focuses on the structural performance. However, additional criteria should be considered in further studies. Water permeability is crucial for water-retaining structures. While the crack behaviour due to loading is discussed, other aspects, such as the influence of the layered structure and imperfections during the fabrication process (see Section 3.3.4), should be investigated. Additionally, the full automation of the process should be further investigated. For this automation, the assembly sequence, e.g. simultaneous printing, placing and spraying as well as more complex geometries, should be considered. A trade-off is most likely necessary for the construction sequence between more complex but faster construction in a simultaneous process and a slower but more robust fabrication with decoupled processes.

7. Conclusions

This study investigated the structural behaviour of 3D printed wall segments reinforced with post-installed reinforcement embedded in sprayed concrete. Five straight specimens with different production parameters and reinforcing bar diameters were subjected to uniaxial tension with eccentric reinforcement. The load-deformation behaviour and crack kinematics of the specimens showed that:

- The overall structural behaviour is independent of the fabrication method and reinforcing bar diameter, with similar ductility as expected for conventional reinforced concrete.
- The unreinforced 3D printed shell does not delaminate from the sprayed one.
- Large out-of-plane deformations occur due to the eccentricity of the reinforcement accompanied by controlled cracking on the surface close to the reinforcement and sudden uncontrolled opening on the opposite side.

The comparison with existing models for the prediction of the stress–strain relationship and crack kinematics revealed that:

- Only part of the cross-section should be considered when modelling the tension stiffening effect to predict the behaviour of eccentrically reinforced concrete members under tension. The best predictions were obtained with an area defined by twice the mechanical cover.
- The most accurate fit is reached for the tension chord model due to the assumption of the highest bond strength.

The observed performance under loading shows that this fabrication approach can be applied for structural shells with one layer of reinforcement. The complex crack behaviour requires further investigation, especially regarding water permeability. Furthermore, different load cases should be considered, and the boundary conditions imposed by a circular wall should be investigated. Such an investigation could be carried out by non-linear finite element modelling or testing a full-scale water tank. While the study focused on the application of circular water tanks, many findings can also be applied to other structures, such as load-bearing shell elements built with this reinforcement approach.

CRediT authorship contribution statement

Lukas Gebhard: Conceptualization, Methodology, Formal analysis, Investigation, Data curation, Writing – original draft, Writing – review & editing. **Jaime Mata-Falcón:** Conceptualization, Methodology, Writing – review & editing, Funding acquisition, Supervision. **Arsalan Iqbal:** Conceptualization, Resources, Writing – review & editing, Funding acquisition. **Walter Kaufmann:** Conceptualization, Writing – review & editing.

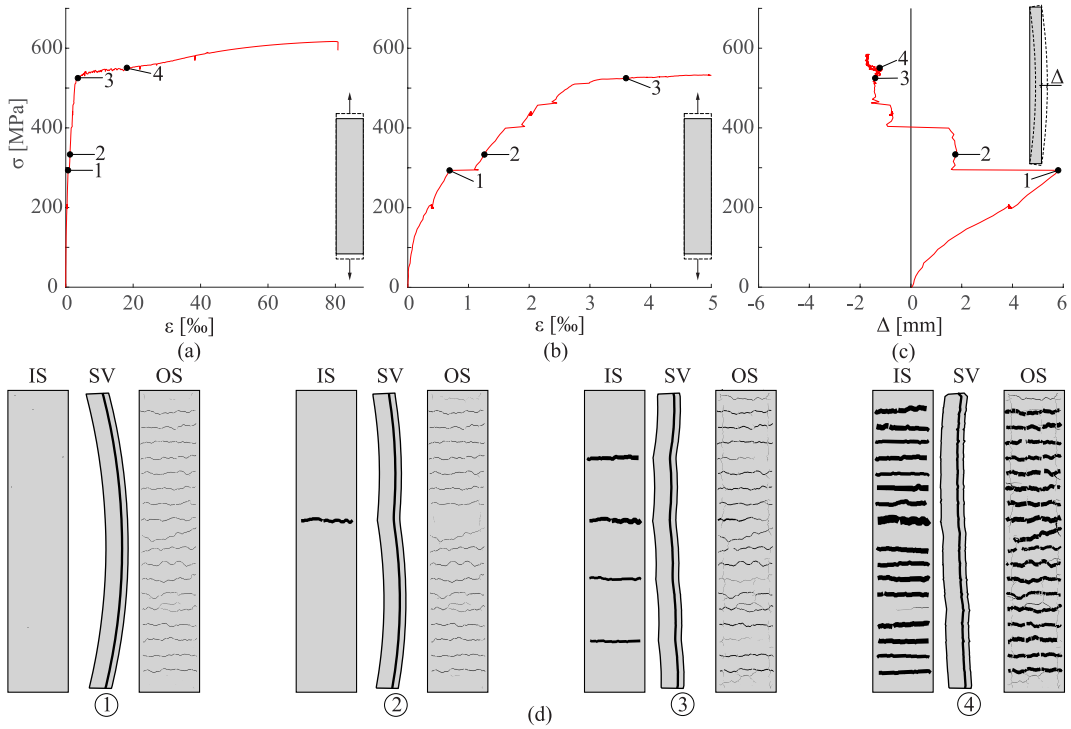

Fig. A1. Load-deformation behaviour and crack formation and kinematics for Specimen 14-sprayed: (a) stress–strain relationship; (b) stress–strain in the cracked-elastic phase; (c) out-of-plane deformations of the centre point; (d) inside (IS), side (SV) and outside (OS) view of the specimen at four characteristic load levels with the crack opening shown on the inside and outside and the deformation in the side view exaggerated by a factor of 20.

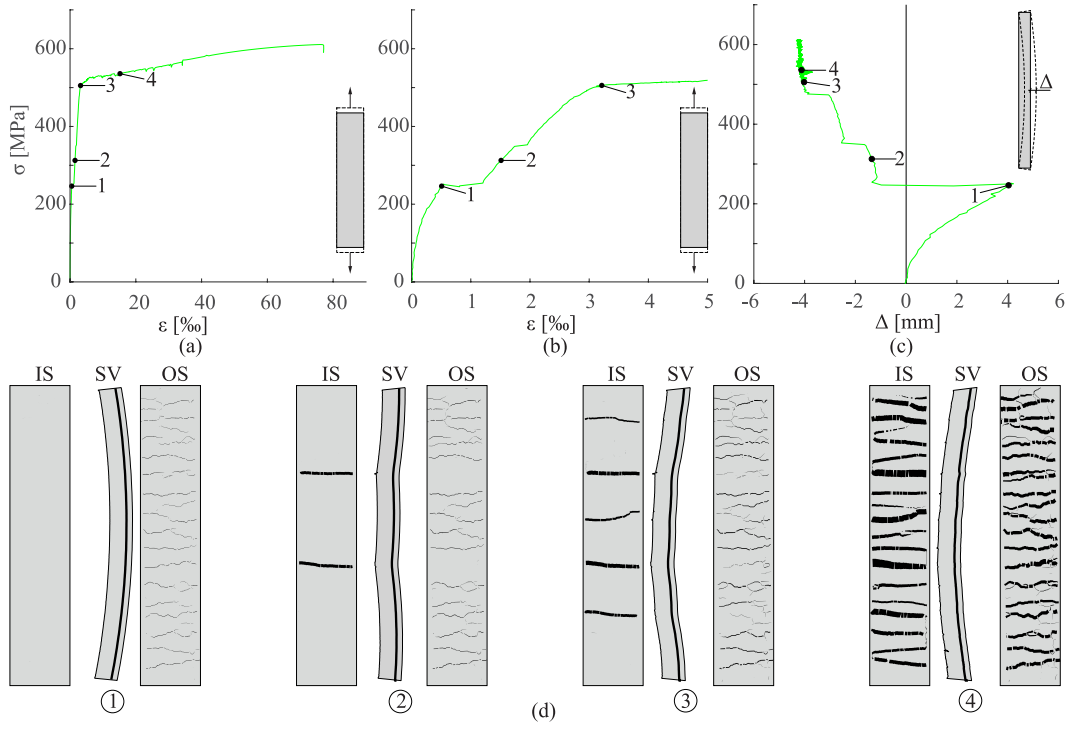

Fig. A2. Load-deformation behaviour and crack formation and kinematics for Specimen 14-3Dp-straight: (a) stress–strain relationships; (b) stress–strain in the cracked-elastic phase; (c) out-of-plane deformations of the centre point; (d) inside (IS), side (SV) and outside (OS) view of the specimen at four characteristic load levels with the crack opening shown on the inside and outside and the deformation in the side view exaggerated by a factor of 20.

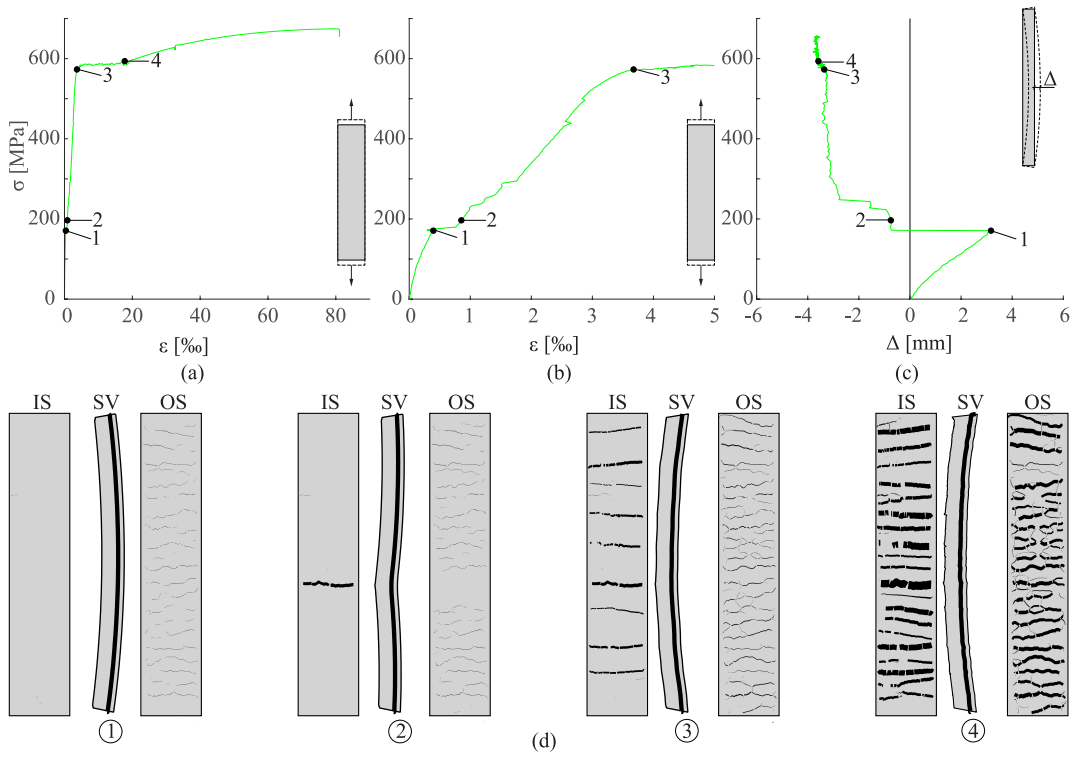

Fig. A3. Load-deformation behaviour and crack formation and kinematics for Specimen 22-3Dp-straight: (a) stress–strain relationship; (b) stress–strain in the cracked-elastic phase; (c) out-of-plane deformations of the centre point; (d) inside (IS), side (SV) and outside (OS) of the specimen at four characteristic load levels with the crack opening shown on the inside and outside and the deformation in the side view exaggerated by a factor of 20.

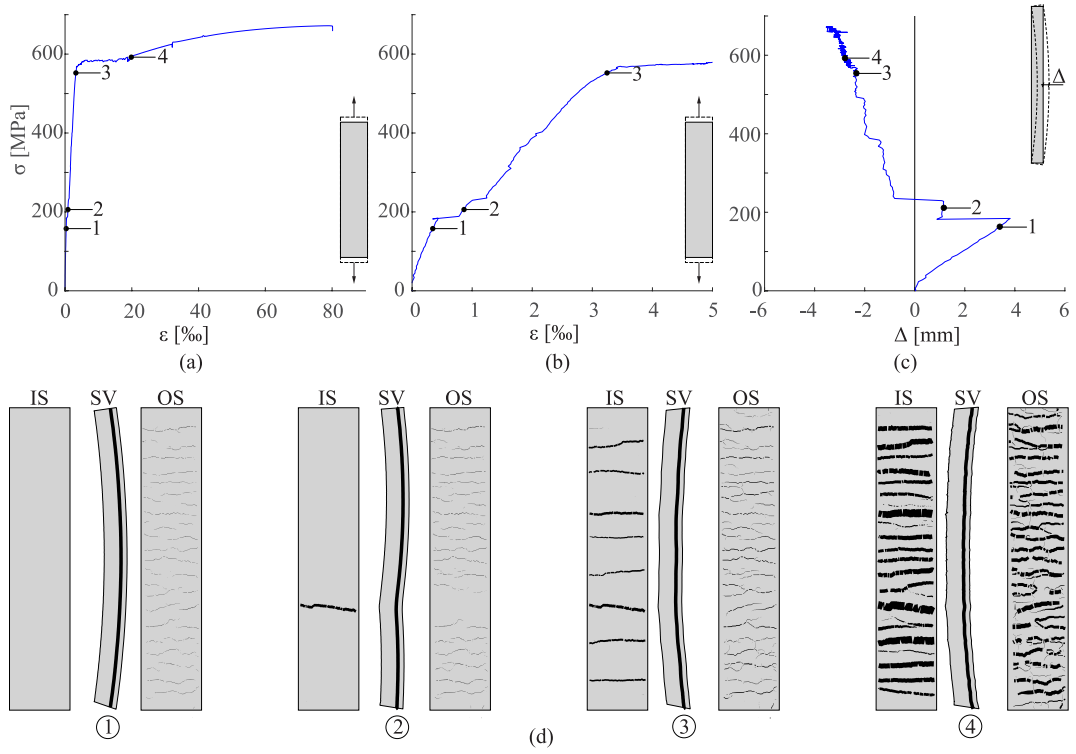

Fig. A4. Load-deformation behaviour and crack formation and kinematics for Specimen 22-3Dp-rough: (a) stress–strain relationship; (b) stress–strain in the cracked-elastic phase; (c) out-of-plane deformations of the centre point; (d) inside (IS), side (SV) and outside (OS) view of the specimen at four characteristic load levels with the crack opening shown on the inside and outside and the deformation in the side view exaggerated by a factor of 20.

Declaration of Competing Interest

The authors declare that they have no known competing financial interests or personal relationships that could have appeared to influence the work reported in this paper.

Data availability

The data for the present publication can be found under the following DOI: https://doi.org/10.3929/ethz-b-000588839

Acknowledgements

The authors would like to express their gratitude to Ana Anton (Digital Building Technologies, ETH Zurich) for her support during printing. Furthermore, the authors are grateful for the support of the teams of the structural laboratory and the Robotic Fabrication Lab. The authors would like to thank Knauf Gips KG for partially funding this study. The experimental campaign was funded by the Swiss National Science Foundation within the National Centre for Competence in Research in Digital Fabrication (project number 51NF40-141853).

Open-access data repository.

The data for the present publication can be found under the following DOI: https://doi.org/10.3929/ethz-b-000588839

Appendix

Appendix A:. Plots of the load-deformation behaviour and crack formation, and kinematics

Appendix B:. Tension chord model for reinforcing steel with a yield plateau and hardening

(extracted from Alvarez [20]).

For the reinforcing steel, three regimes need to be considered:

$$\sigma_s = E_s \cdot \varepsilon_s \qquad \text{for } 0 < \varepsilon_s \leq \varepsilon_{sy} \tag{B1}$$

$$\sigma_s = f_{sy} \qquad \text{for } \varepsilon_{sy} < \varepsilon_s \leq \varepsilon_{sh} \tag{B2}$$

$$\sigma_s = f_{sy} + (f_{su} - f_{sy}) k_c \left[1 - e^{\frac{\varepsilon_{sh} - \varepsilon_s}{\alpha}}\right] \qquad \text{for } \varepsilon_{sh} < \varepsilon_s \leq \varepsilon_{su} \tag{B3}$$

with

$$\alpha = k_a \cdot \frac{\varepsilon_{sh} - \varepsilon_{su}}{\varepsilon_{sh} - k_b} \tag{B4}$$

The factors k_a, k_b and k_c should be adjusted to fit the behaviour of the steel and fulfil the condition

$$\varepsilon_{sh} = k_b + k_a \cdot \ln\left(\frac{k_c - 1}{k_c}\right) \tag{B5}$$

Fig. B.1 shows the resulting model and parameters for the two reinforcing diameters used in this study.

The three regimes of the load-deformation behaviour under uniaxial tension can therefore be described with

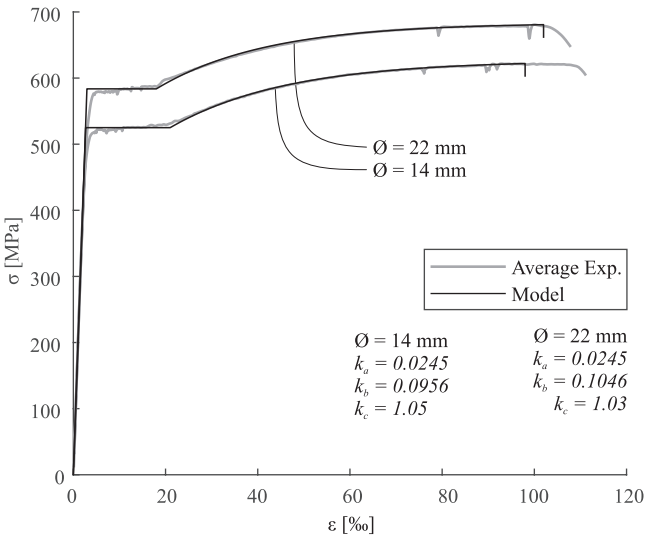

Fig. B1. Modelling of the steel reinforcement used in this study.

$$\varepsilon_{sm} = \frac{\sigma_{sr}}{E_s} - \frac{\tau_{b0} \cdot s_{rm}}{E_s \cdot \varnothing} \qquad \text{for } \sigma_{sr} \leq f_{sy} \text{ (Regime 1)} \tag{B6}$$

$$\varepsilon_{sm} = \frac{\varnothing}{2\tau_{b1} \cdot s_{rm}} \left[\varepsilon_{sh}\left(\sigma_{sr} - f_{sy}\right) + k_c\left(f_{su} - f_{sy}\right)\alpha\{1 + z_1[\ln(z_1) - 1]\}\right] + \frac{s_{rm} - 2x^*}{s_{rm}}\left[\varepsilon_{sy} - \frac{\tau_{b0}(s_{rm} - 2x^*)}{E_s \varnothing}\right] \qquad \text{for } f_{sy} \leq \sigma_{sr} \leq \left(f_{sy} + \frac{2\tau_{b1} \cdot s_{rm}}{\varnothing}\right) \text{ (Regime 2)} \tag{B7}$$

$$\varepsilon_{sm} = \varepsilon_{sh} - \frac{\varnothing}{2\tau_{b1} \cdot s_{rm}} k_c\left(f_{su} - f_{sy}\right)\alpha\{z_2[\ln(z_2) - 1] - z_1[\ln(z_1) - 1]\} \qquad \text{for } \left(f_{sy} + \frac{2\tau_{b1} \cdot s_{rm}}{\varnothing}\right) \leq \sigma_{sr} \leq f_{su} \text{ (Regime 3)} \tag{B8}$$

with

$$x^* = \frac{(\sigma_{sr} - f_{sy})\varnothing}{4\tau_{b1}} \tag{B9}$$

$$z_1 = 1 - \frac{\sigma_{sr} - f_{sy}}{k_c(f_{su} - f_{sy})}, \text{ and } z_2 = 1 - \frac{\sigma_{sr} - f_{sy} - 2\tau_{b1} \cdot s_{rm}/\varnothing}{k_c(f_{su} - f_{sy})} \tag{B10}$$

References

[1] T. Wangler, E. Lloret, L. Reiter, N. Hack, F. Gramazio, M. Kohler, et al., Digital concrete: opportunities and challenges, RILEM Technical Letters 1 (2016) 67–75.

[2] R.A. Buswell, R.C. Soar, A.G. Gibb, A. Thorpe, Freeform construction: mega-scale rapid manufacturing for construction, Autom. Constr. 16 (2007) 224–231.

[3] B. Khoshnevis, Automated construction by contour crafting—related robotics and information technologies, Autom. Constr. 13 (2004) 5–19, http://dx.doi.org/10.1016/j.autcon.2003.08.012.

[4] D. Asprone, C. Menna, F.P. Bos, T.A.M. Salet, J. Mata-Falcón, W. Kaufmann, Rethinking reinforcement for digital fabrication with concrete, Cem. Concr. Res. 112 (2018) 111–121, http://dx.doi.org/10.1016/j.cemconres.2018.05.020.

[5] F.P. Bos, C. Menna, M. Pradena, E. Kreiger, W.R.L. da Silva, A.U. Rehman, et al., The realities of additively manufactured concrete structures in practice, Cem. Concr. Res. 156 (2022), 106746, http://dx.doi.org/10.1016/j.cemconres.2022.106746.

[6] C. Menna, J. Mata-Falcón, F.P. Bos, G. Vantyghem, L. Ferrara, D. Asprone, et al., Opportunities and challenges for structural engineering of digitally fabricated concrete, Cem. Concr. Res. 133 (2020), 106079, http://dx.doi.org/10.1016/j.cemconres.2020.106079.

[7] H. Kloft, M. Empelmann, N. Hack, E. Herrmann, D. Lowke, Reinforcement strategies for 3D-concrete-printing, Civil Eng. Design 2 (2020) 131–139, http://dx.doi.org/10.1002/cend.202000022.

[8] V. Mechtcherine, R. Buswell, H. Kloft, F.P. Bos, N. Hack, R. Wolfs, et al., Integrating reinforcement in digital fabrication with concrete: A review and classification framework, Cem. Concr. Compos. 119 (2021), 103964, http://dx.doi.org/10.1016/j.cemconcomp.2021.103964.

[9] V. Mechtcherine, V.N. Nerella, F. Will, M. Näther, J. Otto, On-site, large-scale, monolithic 3D concrete printing, Constr Print Technol (2020) 14–22.

[10] Lindemann H, Gerbers R, Ibrahim S, Dietrich F, Herrmann E, Dröder K, et al. Development of a Shotcrete 3D-Printing (SC3DP) Technology for Additive Manufacturing of Reinforced Freeform Concrete Structures. In: Wangler T, Flatt RJ, editors. First RILEM International Conference on Concrete and Digital Fabrication – Digital Concrete 2018, Cham: Springer International Publishing; 2019, p. 287–98. Doi: 10.1007/978-3-319-99519-9_27.

[11] V. Mechtcherine, M. Taubert, S. Müller, F. Will, F. Storch, P. Plaschnick, et al., 3D-gedruckte monolithische Stahlbetonwände im CONPrint3D-reinforced Verfahren, Beton- Stahlbetonbau 117 (2022) 235–244, http://dx.doi.org/10.1002/best.202200001.

[12] H.J. Mohammed, Economical design of water concrete tanks, Eur. J. Sci. Res. 49 (2011) 510–520.

[13] D. Asprone, F. Auricchio, C. Menna, V. Mercuri, 3D printing of reinforced concrete elements: Technology and design approach, Constr. Build. Mater. 165 (2018) 218–231, http://dx.doi.org/10.1016/j.conbuildmat.2018.01.018.

[14] F. Bos, R. Wolfs, Z. Ahmed, T. Salet, Large Scale Testing of Digitally Fabricated Concrete (DFC) Elements, in: T. Wangler, R.J. Flatt (Eds.), First RILEM International Conference on Concrete and Digital Fabrication – Digital Concrete 2018, Springer International Publishing, 2019, pp. 129–147.

[15] L. Gebhard, J. Mata-Falcón, A. Anton, B. Dillenburger, W. Kaufmann, Structural behaviour of 3D printed concrete beams with various reinforcement strategies, Eng. Struct. 240 (2021), 112380, http://dx.doi.org/10.1016/j.engstruct.2021.112380.

[16] 3D Printing Platform for Reinforced Printed-Sprayed Concrete Composites vol. 37 (2022) 249–254, http://dx.doi.org/10.1007/978-3-031-06116-5_37.

[17] EN 1992-1-1. Eurocode 2: Design of concrete structures - Part 1-1: General rules and rules for buildings 2004.

[18] EN 1992-3. Eurocode 2: Design of concrete structures - Part 3: Liquid retaining and containment structures 2006.

[19] fib Model Code 2010. fib Model Code for Concrete Structures 2010 2013.

[20] M. Alvarez, Einfluss des Verbundverhaltens auf das Verformungsvermögen von Stahlbeton, ETH Zurich 236 (1998), http://dx.doi.org/10.3929/ethz-a-002000033.

[21] P. Marti, M. Alvarez, W. Kaufmann, V. Sigrist, Tension Chord Model for Structural Concrete, Struct. Eng. Int. 8 (1998) 287–298, http://dx.doi.org/10.2749/101686698780488875.

[22] N. Gehri, J. Mata-Falcón, W. Kaufmann, Automated crack detection and measurement based on digital image correlation, Constr. Build. Mater. 256 (2020), 119383, http://dx.doi.org/10.1016/j.conbuildmat.2020.119383.

[23] N. Gehri, J. Mata-Falcón, W. Kaufmann, Refined extraction of crack characteristics in Large-scale concrete experiments based on digital image correlation, Eng. Struct. 251 (2022), 113486, http://dx.doi.org/10.1016/j.engstruct.2021.113486.

[24] W.F. Chen, Double Punch Test for Tensile Strength of Concrete, ACI J. 67 (1970) 993–995.

[25] P. Marti, Size Effect in Double-Punch Tests on Concrete Cylinders, MJ 86 (1989) 597–601. https://doi.org/10.14359/2261.

[26] Warner, J. Application of thick and heavily reinforced shotcrete. In: Austin S, editor. Sprayed Concrete Technology, E & FN SPON; 2002.

[27] P.M.D. Santos, E.N.B.S. Júlio, A state-of-the-art review on roughness quantification methods for concrete surfaces, Constr. Build. Mater. 38 (2013) 912–923, http://dx.doi.org/10.1016/j.conbuildmat.2012.09.045.

[28] Correlated Solutions. Vic-3D Software Manual 2019.

[29] L. Wang, Y. Yang, L. Yao, G. Ma, Interfacial bonding properties of 3D printed permanent formwork with the post-casted concrete, Cem. Concr. Compos. 128 (2022), 104457, http://dx.doi.org/10.1016/j.cemconcomp.2022.104457.

[30] P. Bischof, J. Mata Falcon, J. Burger, L. Gebhard, W. Kaufmann, Experimental exploration of digitally fabricated connections for structural concrete. (Submitted to), Eng. Struct. (2023).

[31] R. Tepfers, Cracking of concrete cover along anchored deformed reinforcing bars, Mag. Concr. Res. 31 (1979) 3–12, http://dx.doi.org/10.1680/macr.1979.31.106.3.